Nuclear Science and Techniques **24** (2013) 060203

Collimated $LaBr_3$ detector response function in radioactivity analysis of nuclear waste drums

QIAN Nan[1] WANG Dezhong[1,*] WANG Chuan[2]
ZHU Yuelong[2] MAUERHOFER Eric[3]

[1]*School of Nuclear Science and Engineering, Shanghai Jiao Tong University, Shanghai 200240, China*

[2]*Nuclear Power Operations Management Co., Ltd., Haiyan 314300, China*

[3]*Institute of Energy and Climate Research – Nuclear Waste Management, Forschungszentrum Jülich Gmbh, Jülich 52425, Germany*

Abstract The properties of a Lanthanum bromide ($LaBr_3$) detector and its response functions were investigated via experiments and simulations in this paper. The $LaBr_3$ detector had good relative energy resolution and higher efficiency than a high-purity germanium detector. Monte Carlo and other numerical methods were used to calculate the efficiencies of a $LaBr_3$ detector with a square collimation window. A model of the numerical method was established based on a pure geometric model that was consistent with the experimental situation. The results showed that the detector response functions calculated by these methods were in great agreement with experimental results.

Key words Nuclear waste, $LaBr_3$ detector, Detector response, Gamma Scanning, Energy resolution

1 Introduction

The radionuclide activity in radioactive waste drums must be characterized before handling and disposal of them. Segmented gamma scanning (SGS) and tomographic gamma scanning (TGS) are two widely used non-destructive radioactive characterization methods. The accuracy of SGS method is lower than that of TGS method when the waste drum is filled with heterogeneous radioactive materials. However, SGS method consumes less time in measuring a radioactive waste drum compared with TGS[1]. At present, the long measurement time is the biggest constraint on applying TGS in nuclear power plants. Two approaches have been used to reduce the measurement time in TGS—one approach is to establish a new reconstruction algorithm and the other is to use a detector with higher efficiency. Liu used dynamic grids in TGS to reconstruct source distribution[2]. The measurement time was reduced by half, while remains the measurement accuracy. To detect prompt gamma rays from neutro capture, Lanthanum bromide scintillator ($LaBr_3$) was applied to PGNAA[3]. In the present study, a lanthanum bromide ($LaBr_3$) detector was applied to TGS. Its efficiency and energy resolution are described in Section 2. Section 3 discusses the efficiencies of the detector determined by Monte Carlo and deterministic calculation methods. The conclusions are given in Section 4.

2 Properties of $LaBr_3$ crystalline and its detector

2.1 Properties of $LaBr_3$ crystalline

Lanthanum bromide scintillator ($LaBr_3$) with energy resolution of approximately 3% at 662 keV provides a substantial improvement over sodium iodide scintillators in resolution[4]. Unlike HPGe detectors which require low-temperature working conditions, $LaBr_3$ detectors can be operated at room temperature. However, $LaBr_3$ has several disadvantages such as internal radioactivity and low-energy response. The internal radioactivity is due to naturally existing

Supported by Research Fund for the Doctoral Program of Higher Education of China (No.20120073130009), National Natural Science Foundation of China (No.11175118) and Research and innovation project of Shanghai Municipal Education Commission (No.12ZZ022).

* Corresponding author. *E-mail address*: dzwang@sjtu.edu.cn

Received date: 2013-01-14

radioisotopes ^{138}La and decay products of ^{227}Ac[5]. Here, the following properties of a $LaBr_3$ detector were discussed, including Energy linearity, Relative energy resolution, detection efficiency as a function of γ-ray energy.

2.2 Properties of $LaBr_3$ Detector

The $LaBr_3$ crystal was manufactured by Saint–Gobain. The following a set of sources was used in the experiment: ^{133}Ba, ^{152}Eu, ^{137}Cs, ^{60}Co, ^{226}Ra and ^{241}Am. These sources were located at 25 cm away from the detector center, and the measurement time was 3600 s. These sources supplied homogenous and wide range energy of γ-rays, which were used to analyze the ability of $LaBr_3$ detectors and distinguish between the different radionuclides. The experiments primarily aimed to analyze the absolute efficiency, energy linearity, and peak width at half height of the $LaBr_3$ detector. Fig.1 shows a typical spectrum with ^{137}Cs (661.7 keV) and ^{60}Co (1173.21 keV and 1332.47 keV) measured by the $LaBr_3$ detector. Both radioactive sources could be identified, however, the spectrum was affected by the self-activity of the detector (1430 keV from ^{138}La and 1465 keV from ^{40}K) and the 789 keV peak from ^{138}Ce was determined by β-decay. Fig.2 shows a good linearity of the energy from ^{241}Am (59.54 keV) to ^{152}Eu (1408 keV). This energy range covered the most important radioactive sources in the radioactive waste drums. Fig.3 shows the relative energy resolution from ^{241}Am (59.54 keV) to ^{60}Co (1332 keV), which was fitted by the function:

$$\frac{FWHM}{E_\gamma}=\frac{4.94}{E_\gamma}+0.354\sqrt{\frac{1}{E_\gamma}+0.00161} \quad (1)$$

The relative energy resolution is improved from 13% at 59.54 keV to 2% at 1332 keV, which is a satisfactory value for scintillation detectors. Fig.4 shows the full absorption efficiency of the $LaBr_3$ and HPGe detectors from 121 to 1332 keV. ^{60}Co supplied high γ energy, whereas ^{133}Ba and ^{137}Cs supplied low and middle γ energies, respectively. The measurement time was 3 600 s for both detectors, and the count for each peak reached 10 000. The statistical error for each peak was less than 1%. The full absorption efficiency was fitted by Eq.(2).

$$\varepsilon=-\frac{49.12}{E^2}+\frac{0.6919}{E}-1.27\times10^{-4}+3.258\times10^{-7}E-1.607^{-10}E^2 \quad (2)$$

The ratio of the efficiency of the $LaBr_3$ detector to that of the HPGe detector ranged from 1.3 to 2 as energy increased from 121 to 700 keV. The calculated ratio was 2 when energy exceeded 700 keV. Consequently, the measurement time of the $LaBr_3$ detector was the half of that of the HPGe detector.

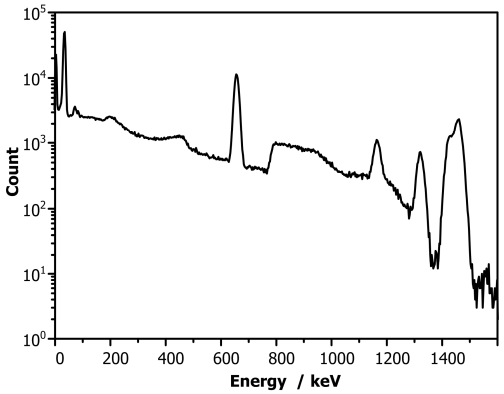

Fig.1 Typical spectrum recorded with a $LaBr_3$ detector using ^{137}Cs and ^{60}Co.

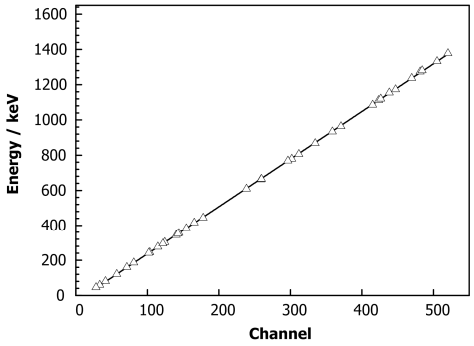

Fig.2 Channel vs. energy data from 59 to 1408 keV for the $LaBr_3$ detector. The solid line denotes a linear fit to the data.

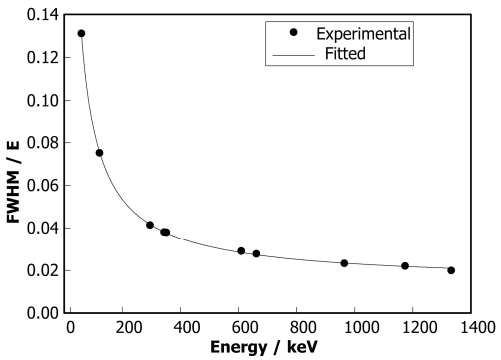

Fig.3 Relative energy resolutions for the $LaBr_3$ detector from 59 to 1332 keV. The solid line represents the fit to the data.

3 Experimental and simulation for the $LaBr_3$ detector response

3.1 Experimental description

In the experiment, the detector was collimated by a square window. The source was distributed on a 9-cm radius circle ($\mathbf{r_s}$) in front of the detector. The distance (d_0) between the circular center and the detector was 52 cm. Fig.5 schematically illustrates the experimental setup of the collimated detector system. The crystal is 1.96 cm in radius (r_d) and 3.91 cm in length. The collimator is 12 cm in length (l_{col}), and its square window (a_{col}) is 4.8 cm in width. The drum was rotated in steps. The source located at 9 and 20 cm radial positions to a location shifted 3.5 cm (l) to the drum center. A photon count rate was measured and the drum was rotated for 15° in each step.

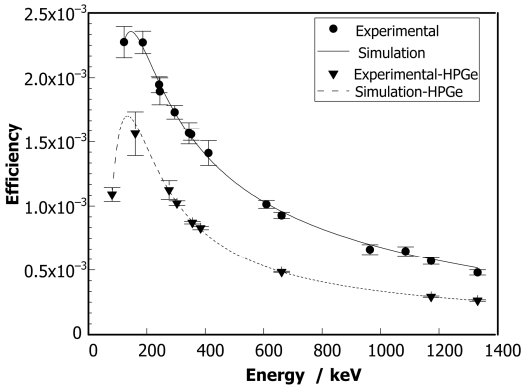

Fig.4 Efficiencies for $LaBr_3$ and HPGe detectors from 59 to 1332 keV. The solid and dashed lines denote the fit to the data.

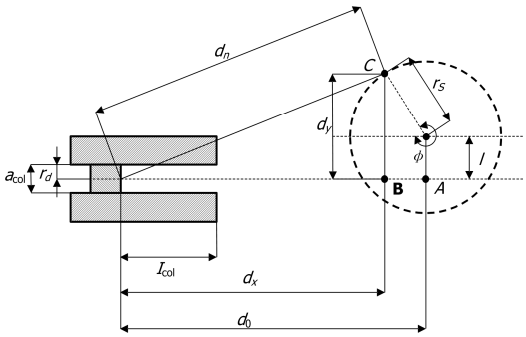

Fig.5 Geometric model of the collimated detector system of the experiment. l: the offset between the center of the source circle and the axis of the detector; A: the projection of the center of the source circle on the axis of the detector; B: the projection of the point source C on the axis of the detector; d_x: the distance between the point source C and detector surface; d_y: the distance between the point source C and the axis of the detector; d_n: the distance between the point source C and detector surface center; d_0: the distance between point A and the detector surface; and φ: the angle of the point source.

3.2 MCNP simulation of the $LaBr_3$ detector response

This section presents the results of the simulations of the $LaBr_3$ detector response using the Monte Carlo *N*-particle (MCNP) method. The efficiencies of the sources in different positions are basic parameters in gamma scanning techniques. It was difficult to determine the efficiencies via experiments because the energy from experimental sources cannot cover all energies in the waste drum. By contrast, the energies and positions of the point sources as well as the void sources can be easily established in the simulation model. Thus, experiments can be replaced by simulations to a certain extent.

In Fig.6, the simulated values are compared with the experimental results. A good agreement between the experimental and the simulated efficiencies is obtained. The average error is less than 3%, indicating that the simulation model can fit the experimental results very well.

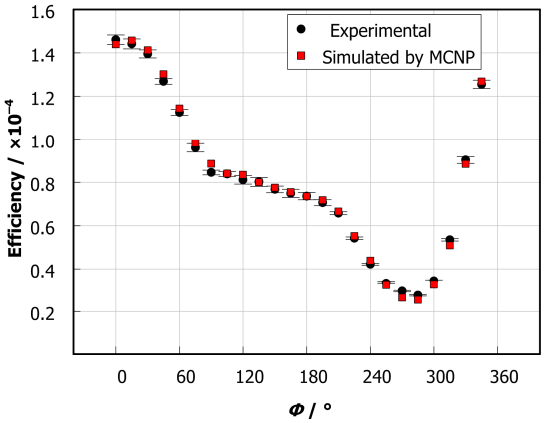

Fig.6 Comparison of the experimental results (circle points) with the simulation efficiencies by MCNP (square points) for ^{137}Cs point source (E_γ = 0.661 MeV).

3.3 Simulation of the $LaBr_3$ detector response by the numerical method

3.3.1 Numerical method

Although MCNP simulation can fit the experimental results, it needs a long time to calculate the detector efficiency. By contrast, the numerical method significantly decreases the calculation time. For example, it takes about 9 minutes to calculate the efficiency of one point by MCNP while only 5 minutes to calculate the efficiency of 90 points by numerical

method using the same computer. Thus, the numerical method may replace the MCNP. A calculation model for a point source is shown in Fig.5. The detector efficiency can be calculated based on the solid angle subtended by the collimated detector to the point source. Fig.5 presents geometry in accordance with Krings and Mauerhofer (2011)[6] as well as Nan et al. (2012)[7]. The absolute detector efficiency $\varepsilon(d_n)$ to the point source can be calculated by

$$\varepsilon(d_n)=\varepsilon(d_0)\cdot\left(\frac{d_0}{d_x}\right)^m\cdot\frac{S_{dn}}{S_{det}}\cdot Cor \tag{3}$$

where $\varepsilon(d_n)$ is the absolute detector efficiency to a point source located at the distance d_n to the detector; $\varepsilon(d_0)$ is the absolute detector efficiency of a point source located at the drum center; $S_{\rm dn}$ is the part of the active detector surface illuminated by the photon beam due to the collimation; $S_{\rm det}$ is the area of the active detector surface; C is correction factor of edge penetration effect; m is the power of (d_0/d_x).

The efficiencies were calculated based on the efficiency of the source located at Point A. First, the efficiency of point A was transformed to Point B located at d_n (Fig.5). This transformation mainly depended on the distance between the point source and the detector surface. Then, the efficiency of Point B was transformed to the target location (Point C). This transformation mainly depended on the active detector surface illuminated by the photon beam S_{dn}. The factor Cor corrected the absolute efficiency considering the edge penetration effect. Unscattered part of the photon beam that passed through the collimator and reached the active detector volume were disregarded because they had negligible effects on the transformation of the efficiencies. The source was divided into large point sources when the source was a volume source. The efficiency of this volume source ε represents the average efficiencies of the point sources. The efficiency ε is calculated by

$$\varepsilon=\frac{1}{k}\sum_{i=1}^{k}\varepsilon(d_0)\cdot\left(\frac{d_0}{d_x^i}\right)^m\cdot\frac{S_{dn}^i}{S_{det}}\cdot Cor^i \tag{4}$$

where k is the number of point sources in the volume source.

3.3.2 Illuminated active detector surface

In this section, r_d is the radius of the active detector surface. Fig.7 presents six cases of the schematic calculation of $S_{\rm dn}$ referring to Nan et al. (2012)[7]. Before calculating $S_{\rm dn}$ in these cases, the arc segment areas (S) must be calculated. The area of an arc segment according to the notation used in Fig.5 is given by

$$S=\frac{r_d^2\delta}{2}-\frac{g}{2}\cos\frac{\delta}{2}r_{\rm d}\,, \tag{5}$$

where g is the length of the chord given by the intersection of the active detector surface and one side of the collimated photon beam. The central angle of the sector is expressed as

$$\delta=2\arcsin\frac{g}{2r_{\rm d}} \tag{6}$$

The side length of the photon beam at the plane defined by the active detector surface is given by

$$a_{\rm pro}=\frac{l_{\rm col}}{d_x-l_{\rm col}}\times a_{\rm col} \tag{7}$$

where d_x is the projection of d_n on the X-axis. According to Eqs. 5-7 and Fig.7, $S_{\rm dn}$ for these cases can be calculated by

$$S_{\rm dn}=\begin{cases}0 & \text{case 1}\\ \pi r_{\rm d}^2 & \text{case 2}\\ S_1+\frac{1}{2}\left|a_y-b_y\right|\left|a_z-b_z\right| & \text{case 3}\\ \pi r_d^2-(S_1+S_2) & \text{case 4}\\ S_1 & \text{case 5}\\ \pi r_{\rm d}^2-S_1 & \text{case 6}\end{cases} \tag{8}$$

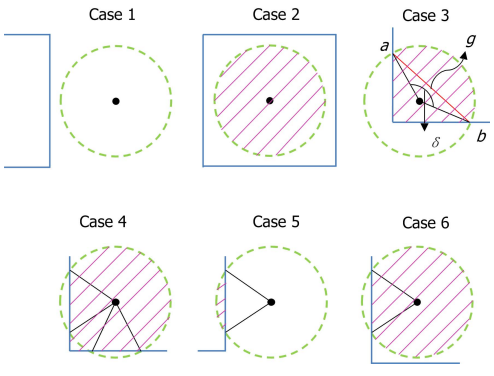

Fig.7 Active detector surface illuminated by the photon beam using a square collimation. $S_{\rm i}$: arc segment areas in different cases.

3.3.3 Edge penetration correction

Fig.8 schematically presents different path lengths of photons in a detector crystal from a point source. The

correction factor was calculated as the average absorption probability of the photon beam with respect to the average absorption probability of a photon beam from a point source facing the detector. The calculation of the average absorption probability relied on a mesh of n_0 virtual points distributed homogenously at the active detector surface. The penetration lengths $l_i\mathbf{r_s}$ of photons from a point source were calculated for each photon beam that entered the active detector surface at one of the n points within the illuminated part of the active detector surface. The correction factor can be expressed as

$$Cor=\left(1-\frac{1}{n}\sum_{i=1}^{n}\mathrm{e}^{-\frac{\mu}{\rho}\rho l_i\mathbf{r_s}}\right)\cdot\left(1-\frac{1}{n_0}\sum_{i=1}^{n_0}\mathrm{e}^{-\frac{\mu}{\rho}\rho l_i(\vec{r}_s)}\right)^{-1} \quad (9)$$

n: the number of virtual points distributed at the active detector surface in different conditions; μ: the linear attenuation coefficient of Ge; ρ: the density of the Ge; n_0: the maximal number of virtual points distributed at the active detector surface.

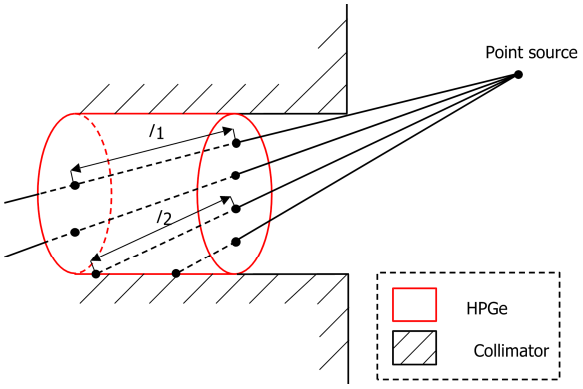

Fig.8 Scheme of the different penetration lengths of photons from a point source in a collimated detector crystal.

3.3.4 Parameter *m*

The detector efficiency ε is determined by the detector intrinsic efficiency $\varepsilon_{\mathrm{det}}$ and the detector spatial efficiency $\varepsilon_{\mathrm{spa}}$

$$\varepsilon=\varepsilon_{\mathrm{det}}\times\varepsilon_{\mathrm{spa}} \quad (10)$$

The detector spatial efficiency $\varepsilon_{\mathrm{spa}}$ is proportional to the solid angle of the cone formed by the point source and the detector surface.

$$\varepsilon_{\mathrm{spa}}=\frac{1}{2}\left(1-\cos\frac{\theta}{2}\right) \quad (11)$$

where θ represents the solid angle of the cone formed by the point source and the detector surface. According to Taylor series expansion,

$$\varepsilon_{\mathrm{spa}}=\frac{1}{4}\left(\frac{\theta}{2}\right)^2-\frac{1}{8\times4!}\left(\frac{\theta}{2}\right)^4+O\left(\frac{\theta}{2}\right) \quad (12)$$

when $d_x >> r_d$, θ is expressed by

$$\theta\approx\frac{2r_d}{d_x} \quad (13)$$

$$\varepsilon=\frac{\varepsilon_{\mathrm{det}}r_d^2}{4}\cdot\frac{1}{d_x^2} \quad (14)$$

$$\frac{\varepsilon_{\mathrm{A}}}{\varepsilon_{\mathrm{B}}}=\left(\frac{d_0}{d_x}\right)^{-2} \quad (15)$$

The distance between the source and the detector surface is always larger than the radius of the detector. According to Eqs. 3, m was

$$m=\frac{\ln\left(\frac{\varepsilon_{\mathrm{A}}}{\varepsilon_{\mathrm{B}}}\right)}{\ln\left(\frac{d_0}{d_x}\right)}$$

Thus, the value of m equalled –2

3.3.5 Reliability analysis of numerical method

The count rate distribution of ^{137}Cs point sources was simulated under the same experimental condition. The experimental and calculated results about the count rate are shown in Fig.9. The calculated results were in a good agreement with the experimental results for all simulated source positions. The average error was less than 3%. This verifies the rationale of the numerical method in simulation of the $LaBr_3$ detector response.

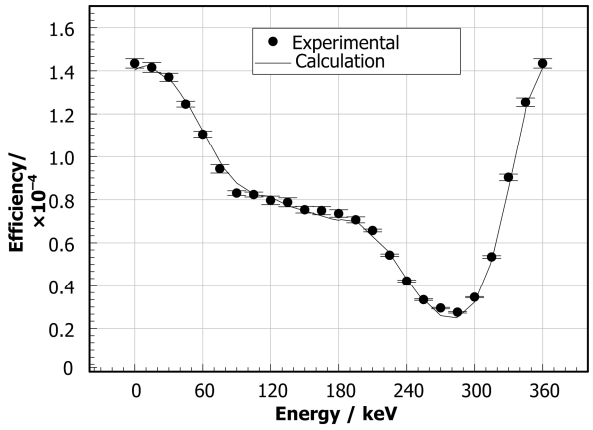

Fig.9 Comparison between the experimental results (symbols) to calculation efficiencies according to the model (line) for ^{137}Cs point source (E_γ = 0.661 MeV).

4 Conclusion

This study demonstrated that the $LaBr_3$ detector can be used in SGS and TGS techniques. The error between the experimental results and the MCNP simulation results in the detector efficiencies was less than 3%. The numerical method used to calculate the response of the $LaBr_3$ detector geometry of the gamma scanning systems agreed perfectly with the experimental data. Therefore, the numerical method of the $LaBr_3$ detector response can be used in SGS and TGS techniques.

References

1. Tran Q D. Ann Nucl Energy, 1997, **24:** 33–47.
2. Liu C, Gu W G, Qian N, *et al*. Nucl Sci Tech, 2012, **23:** 277–283.
3. Van Loef E V D, Dorenbos P, Van Eijk C W E, *et al*. Appl. Phys. Lett, 2001, **79:** 1573–1575.
4. Favalli A, Mehner H C, Ciriello V, *et al*. Appl Radiat Isotopes, 2010, **68:** 901–904.
5. Milbrath, Brian D, McIntyre, Justin I, *et al*. Contamination in $LaCl_3$:Ce Scintillators. Richland: Pacific Northwest National Laboratory, 2005, 1–15.
6. Thomas K, Eric M. Appl. Radiat. Isot, 2011, **69:** 880–889.
7. Nan Q, Thomas K, Eric M, *et al*. J Radioanal Nucl Ch, 2012, **292:** 1325–1328.